Genetic deletion of Nox4 enhances cancerogen-induced formation of solid tumors

Valeska Helfinger[a], Florian Freiherr von Gall[a], Nina Henke[b], Michael M. Kunze[b], Tobias Schmid[b], Flavia Rezende[a], Juliana Heidler[c], Ilka Wittig[c,d], Heinfried H. Radeke[e], Viola Marschall[f], Karen Anderson[g], Ajay M. Shah[h], Simone Fulda[f], Bernhard Brüne[b], Ralf P. Brandes[a], and Katrin Schröder[a,1]

[a]Institute for Cardiovascular Physiology, Goethe University, 60590 Frankfurt am Main, Germany; [b]Institute for Biochemistry I/ Pathobiochemistry, Goethe University, 60590 Frankfurt am Main, Germany; [c]Functional Proteomics, SFB 815 Core Unit, Goethe University, 60590 Frankfurt am Main, Germany; [d]Cluster of Excellence "Macromolecular Complexes," Goethe University, 60590 Frankfurt am Main, Germany; [e]Pharmazentrum Frankfurt, Goethe University, 60590 Frankfurt am Main, Germany; [f]Institute for Experimental Cancer Research in Pediatrics, Goethe University, 60590 Frankfurt am Main, Germany; [g]Signaling Department, The Babraham Institute, Cambridge CB22 3AT, United Kingdom; and [h]Cardiovascular Division, King's College London British Heart Foundation Centre, London WC2R 2LS, United Kingdom

Edited by Navdeep S. Chandel, Northwestern University, Chicago, IL, and accepted by Editorial Board Member Tak W. Mak January 25, 2021 (received for review September 30, 2020)

Reactive oxygen species (ROS) can cause cellular damage and promote cancer development. Besides such harmful consequences of overproduction of ROS, all cells utilize ROS for signaling purposes and stabilization of cell homeostasis. In particular, the latter is supported by the NADPH oxidase 4 (Nox4) that constitutively produces low amounts of H_2O_2. By that mechanism, Nox4 forces differentiation of cells and prevents inflammation. We hypothesize a constitutive low level of H_2O_2 maintains basal activity of cellular surveillance systems and is unlikely to be cancerogenic. Utilizing two different murine models of cancerogen-induced solid tumors, we found that deletion of Nox4 promotes tumor formation and lowers recognition of DNA damage. Nox4 supports phosphorylation of H2AX (γH2AX), a prerequisite of DNA damage recognition, by retaining a sufficiently low abundance of the phosphatase PP2A in the nucleus. The underlying mechanism is continuous oxidation of AKT by Nox4. Interaction of oxidized AKT and PP2A captures the phosphatase in the cytosol. Absence of Nox4 facilitates nuclear PP2A translocation and dephosphorylation of γH2AX. Simultaneously AKT is left phosphorylated. Thus, in the absence of Nox4, DNA damage is not recognized and the increased activity of AKT supports proliferation. The combination of both events results in genomic instability and promotes tumor formation. By identifying Nox4 as a protective source of ROS in cancerogen-induced cancer, we provide a piece of knowledge for understanding the role of moderate production of ROS in preventing the initiation of malignancies.

solid tumors | Nox4 | AKT | genomic instability

Reactive oxygen species (ROS) cause aging, detrimental alterations of cell homeostasis, and are a precaution of cancer. Nevertheless, prospective randomized clinical trials on antioxidant supplementation have failed to provide protection from cancer and in some studies antioxidants even increased the risk of a negative outcome (1, 2). More than 25 y ago, the ATBC trial of dietary supplementation of male smokers with the antioxidants alpha-tocopherol or beta-carotene for several years revealed no reduction in the incidence of lung cancer. Instead those supplements may have harmful effects (3). Later, in 2011, the SELECT trial even suggested that dietary supplementation with vitamin E significantly increased the risk of prostate cancer among healthy men (4). Animal experiments demonstrated that some major antioxidants of clinical use, such as *N*-acetylcysteine and vitamin E, accelerate progression of lung cancer in mice carrying mutations in K-Ras and B-Raf (5) and therefore may not serve as appropriate therapeutics for existing cancers.

A potential explanation for these findings is that ROS are not just a representation of environmental stress or inflammation. Rather all cells produce ROS for signaling purposes. ROS for signaling purposes have to be generated in a highly controlled manner, as facilitated by the Nox family of NADPH oxidases (6). Nox-dependent ROS production in general occurs in response to cellular stimulation and subsequent increases in intracellular calcium or activation of Rac and protein kinase C (7). There is however one exception, the NADPH oxidase Nox4. This enzyme constitutively produces low amounts of H_2O_2 and thus its output is controlled by its expression level.

The microenvironment of solid tumors is often characterized by hypoxic conditions and increased abundance of cytokines such as TGFβ, both potent inducers of Nox4 expression (8, 9). As a consequence of cellular stress and increased ROS formation, expression of tumor suppressor genes, such as Nrf2, are induced for facilitating antioxidative responses and cellular protection (10). Indeed, Nox4 maintains the expression of Nrf2 (11). Absence of Nox4 in mice results in a hyperinflammatory phenotype (11–15). Further, Nox4 expression is induced in the course of differentiation and is essentially involved in differentiation of mesenchymal cells (16–18). Cell stress, dedifferentiation, and inflammation are well-established prerequisites for malignant transformation and accordingly, we hypothesized that knockout of Nox4 increases the risk of cancer development.

Significance

The stereotype of ROS produced by NADPH oxidases as cause of malignant diseases persists in a generalized manner. In fact, high levels of ROS formation could be harmful in the context of a disease process. This study demonstrates that loss of the NADPH oxidase Nox4, as a constitutive source of ROS, promotes cancerogen-induced formation of solid tumors. Accordingly, a certain tonic, constitutive low level of Nox4-derived hydrogen peroxide appears to reduce the risk of cancerogen-induced tumor formation.

Author contributions: K.S. designed research; V.H., F.F.v.G., N.H., M.M.K., F.R., J.H., I.W., V.M., K.A., and K.S. performed research; N.H., M.M.K., T.S., J.H., I.W., H.H.R., V.M., K.A., A.M.S., S.F., B.B., and R.P.B. contributed new reagents/analytic tools; V.H., F.F.v.G., N.H., M.M.K., T.S., J.H., I.W., V.M., K.A., and K.S. analyzed data; and K.S. wrote the paper.

The authors declare no competing interest.

This article is a PNAS Direct Submission. N.S.C. is a guest editor invited by the Editorial Board.

[1]To whom correspondence may be addressed. Email: schroeder@vrc.uni-frankfurt.de.

This article contains supporting information online at https://www.pnas.org/lookup/suppl/doi:10.1073/pnas.2020152118/-/DCSupplemental.

Published March 8, 2021.

Results

Loss of Nox4 Promotes Tumor Development. In order to determine the impact of Nox4 on tumor development, two different cancerogen-induced and inflammation-driven cancer models in Nox4 knockout mice were analyzed. When compared with wild-type (WT) mice, Nox4 knockout mice develop twice as many tumors in the azoxymethane/dextran sulfate sodium (AOM/DSS) colon carcinoma model (Fig. 1 *A*–*C*). Similar results were obtained in a second model of fibrosarcoma development in response to subcutaneous 3-methylcholanthrene (MCA) injection. In Nox4$^{-/-}$ mice, onset of tumor development was earlier and developing tumors grew faster than in WT animals (Fig. 1 *D*–*F*). Proliferation in both tumor models was more than doubled in Nox4$^{-/-}$ mice when compared with WT mice (Fig. 1 *G* and *H*).

Importantly, these effects were specific for Nox4: Deletion of Nox1 rather had an inhibitory effect on tumor development, and deletion of Nox2 was without effect at all (*SI Appendix*, Fig. S1). In order to exclude unknown effects of adaptation to life-long Nox4 deficiency as a reason for more tumor development, conditional Nox4 knockout mice with tamoxifen-inducible deletion of Nox4 were studied in the MCA model. Although systemic administration of tamoxifen increased the number of Nox4 flox/flox control animals with sarcoma, the relative increase in tumor development in tamoxifen-induced systemic Nox4 knockouts was comparable to Nox4$^{-/-}$. Conditional deletion of Nox4 in macrophages or endothelial cells, in contrast, was without effect on tumor development, suggesting that most likely Nox4 in the transforming cells but not in the tumor stroma mediates the protective effect. Indeed, when we performed similar experiments in fibroblast and enterocyte-specific Nox4$^{-/-}$ mice, formation of both kinds of tumors (sarcoma and carcinoma) was enhanced (*SI Appendix*, Fig. S2). Whether the effect of Nox4 deficiency on proliferation seen in this study is a consequence of an earlier onset of tumor formation or faster proliferation of the tumor cells when missing Nox4 remains elusive (*SI Appendix*, Fig. S3). The effect of Nox4 on proliferation is discussed controversially (14, 19–21). Conflicting results suggest that unknown differences in the cell culture of different laboratories influence the results. Tumor growth and progression can result from many effects

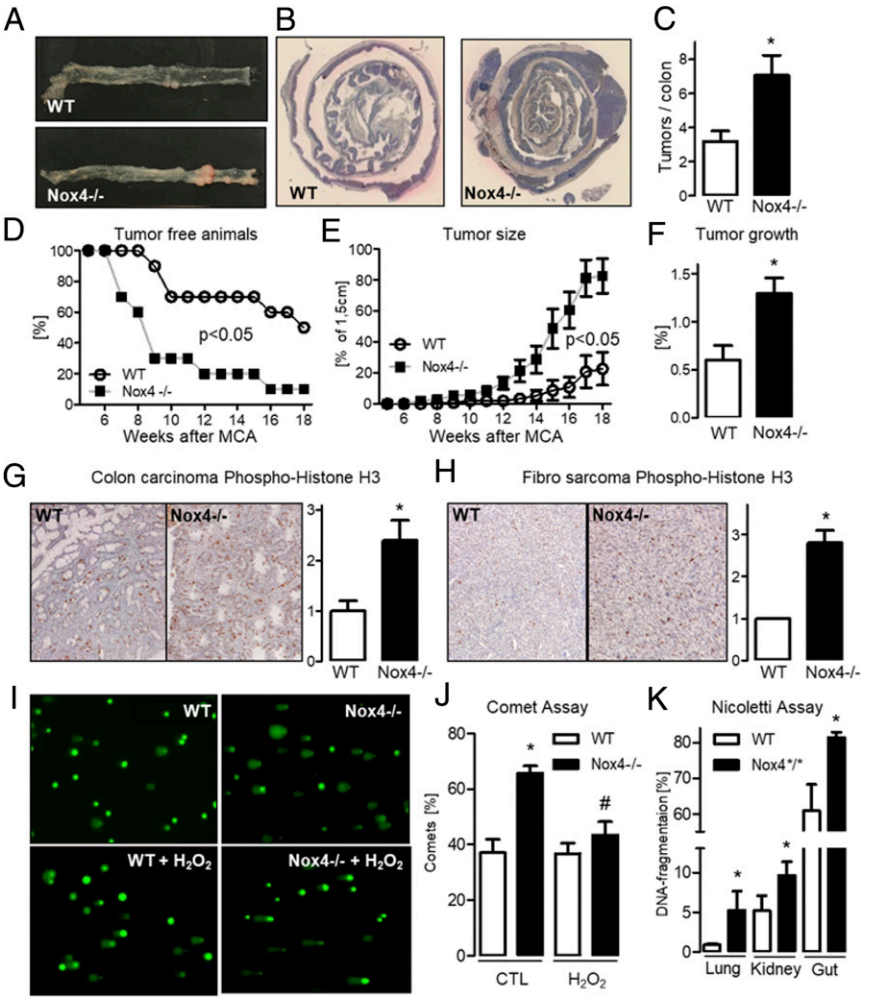

Fig. 1. Nox4 knockout promotes tumor development and induces genomic instability. (*A*–*C*) AOM-DSS colon carcinogenesis model: Representative macro photo (*A*), H&E overview (*B*), and average number of solid carcinoma nodules (*C*) in the colon induced by AOM/DSS. (n = 11), *P < 0.05 (*D*–*F*) MCA fibrosarcoma model. Fibrosarcoma development (*D*), tumor size (*E*) (100% equals the maximal tumor size of 1.5 cm, n = 10), and relative tumor growth (*F*). (*G* and *H*) Colon carcinomas and sarcomas stained for phosphorylated histone H3 (pH3) as proliferation marker. The statistics indicate the relative staining intensity (n = 5 to 9). (*I* and *J*) Measurement of DNA double-strand breaks in fibrosarcoma cells was performed using comet assay (n = 5). Comet assay of cells treated with or without H_2O_2 (24 h, 5 μM). Original pictures (*I*) and statistics (*J*) *P < 0.05; WT vs. Nox4$^{-/-}$, #P < 0.05 CTL vs. H_2O_2 treated. (*K*) Conditional tamoxifen-inducible knockout mice were treated with tamoxifen for 10 d and 1 wk later cells were isolated from multiple organs and analyzed for DNA fragmentation by Nicoletti assay (n = 3).

without significant individual impact, which nevertheless in vivo sum up to significant differences that highly influence tumor progression.

Knockdown of Nox4 Results in Genomic Instability. Genomic instability is an important factor to promote tumor development. Cell lines from WT and Nox4 tumors were established and comet assays for detection of DNA fragmentation were performed. Nox4 knockout tumor cells exhibited a doubling in the number of comets, which indicate DNA double-strand breaks. This effect was reversible, when the tumor cells were treated with H_2O_2 (5 μmol/L, 24 h) in Nox4$^{-/-}$ tumor cells, whereas comet formation in WT tumor cells remains equal (Fig. 1 *I* and *J*). These observations suggest that lack of Nox4-derived H_2O_2 may promote genomic instability. Indeed, Nicoletti staining of lung, liver, and intestine of healthy Nox4$^{-/-}$ mice demonstrated that DNA strand breaks are more frequent after deletion of Nox4 even in normal tissue (Fig. 1*K*).

Loss of Nox4 Results in Attenuated Recognition of DNA Damage. Increased DNA fragmentation could be a consequence of more DNA damage or less DNA damage repair. Overwhelming ROS formation can induce DNA damage. However, knockout of Nox4 reduced the level of AmplexRed-detectable H_2O_2, and no major difference in other ROS was found (*SI Appendix*, Fig. S4). Total glatathion (GSH) and oxidized glutation (GSSG) were similar in Nox4$^{-/-}$ and wild-type, while the GSH/GSSG ratio was reduced in Nox4-deficient cells (*SI Appendix*, Fig. S5). We conclude that DNA fragmentation in Nox4$^{-/-}$ is not a consequence of ROS-induced DNA damage. Despite more DNA fragmentation, phosphorylation of histone 2AX (γH2AX) as a marker of DNA damage decreased in tumors and tumor cells of Nox4$^{-/-}$ mice when compared with WT mice. Accordingly, although DNA fragmentation was enhanced in healthy colon cells and fibroblasts of Nox4$^{-/-}$ mice, γH2AX abundance was lower than in wild-type cells (Fig. 2 *A–D*). Further, acute exposure of fibroblasts to the carcinogen MCA increased γH2AX less effectively in Nox4$^{-/-}$ cells then in WT cells (Fig. 2*D*). Expression and activity of the kinase ATM, which phosphorylates H2AX in response to damage and initiates the DNA damage response, was not reduced in Nox4-deficient cells (*SI Appendix*, Fig. S6). ATM kinase also is a key molecule that stabilizes p53 after DNA damage. Despite a normal function of ATM, but in line with the missing induction of γH2AX, p53 protein and mRNA expression were reduced in Nox4 knockout tumors and cells (Fig. 2 *E–H*). Treatment with H_2O_2, the product of Nox4, normalized p53 mRNA expression in Nox4-deficient cells but had no effect in WT cells (Fig. 2*F*). Importantly, the decreased p53 expression was not a consequence of altered phosphorylation or translation of p53 (*SI Appendix*, Fig. S7 *A–D*) nor was the expression of enzymes involved in p53 degradation, like NQO1 and MDM2, increased in Nox4$^{-/-}$ cells (*SI Appendix*, Fig. S7 *E* and *F*). In order to study whether the reduced p53 expression is a consequence of an inappropriate response to DNA damage, healthy lung endothelial cells from WT and Nox4$^{-/-}$ mice were stimulated with the carcinogen MCA. This treatment strongly induced p53 expression in WT but not in Nox4$^{-/-}$ cells (Fig. 2*I*). These

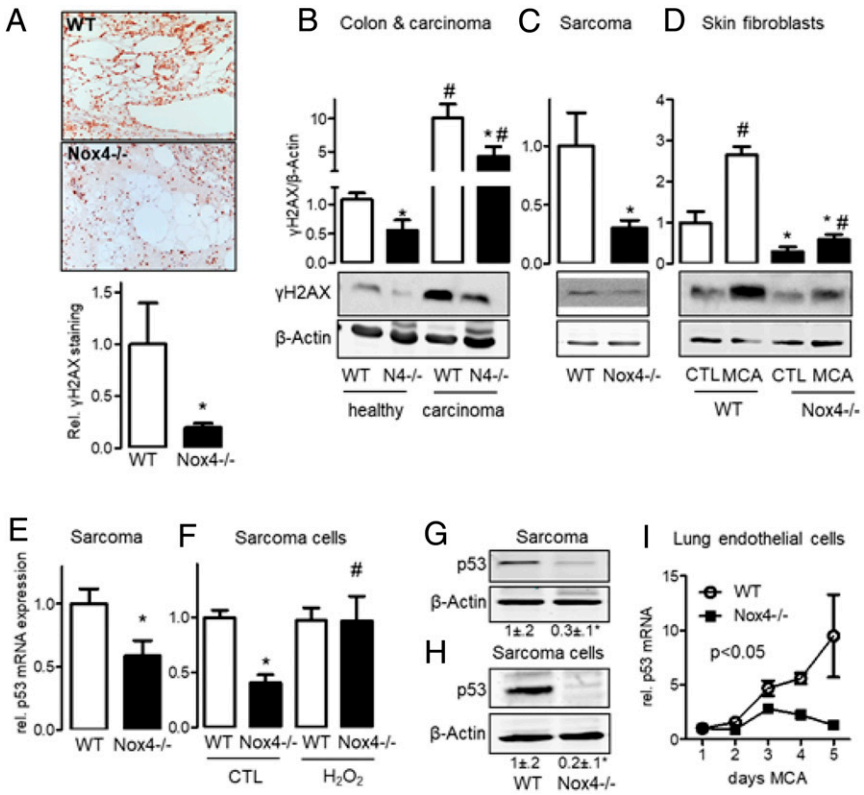

Fig. 2. Nox4 deficiency results in an enhanced DNA instability. (*A*) Cross-sections of the skin of WT and Nox4$^{-/-}$ mice stained for phosphorylated H2AX 20 d after MCA injection as a sign of DNA damage. (*B* and *C*) Western blot for the expression of the DNA damage marker γH2AX from (*B*) healthy colon and colon carcinomas ($n = 11$ WT and 9 Nox4$^{-/-}$) and (*C*) fibrosarcoma tissue ($n = 4$). (*D*) Western blot for γH2AX in primary skin fibroblasts treated with or without MCA for 3 d (5 μg/mL, $n = 3$). *$P < 0.05$ WT vs. Nox4$^{-/-}$, #$P < 0.05$ WT/Nox4$^{-/-}$ healthy/CTL vs. WT/Nox4$^{-/-}$ carcinoma/MCA. (*E–H*) p53 abundance. mRNA (*E* and *F*) and protein (*G* and *H*) of p53 in fibrosarcoma tissue (*E* and *G*) and isolated fibrosarcoma cells (*F* and *H*). Numbers below the blots are the results of the densitometry. *$P < 0.05$. $n > 5$. H_2O_2 denotes treatment with 5 μM for 24 h. (*I*) p53 mRNA expression was measured by RT-qPCR after MCA treatment (1 to 5 d, 5 μg/mL) in freshly isolated lung endothelial cells ($n = 5$).

data indicate a general attenuation of DNA damage response in the absence of Nox4.

Nox4 Deficiency Enhances Nuclear PP2A Activity. Steady-state levels of γH2AX are raised by the kinase ATM and reduced by serine-threonine phosphatases of the PP2A family (22, 23). Given the normal ATM expression and activity, we hypothesized that PP2A activity is altered in Nox4$^{-/-}$ cells. Indeed, by proximity ligation assay (PLA) with a pan-C subunit antibody for the PP2A family an increased association of a PP2A member with γH2AX in the nucleus was observed (Fig. 3*A*). Whereas the total cellular expression of PP2A was similar in WT and Nox4$^{-/-}$ cells, a shift toward more nuclear PP2A was observed in Nox4$^{-/-}$ cells (Fig. 3*B*). Consequently, global serine-threonine phosphatase activity was decreased in the cytosol and increased in the nucleus of Nox4$^{-/-}$ cells, when compared with the corresponding WT cells (Fig. 3*C*). In order to verify that an increased nuclear PP2A activity causes reduced γH2AX abundance, experiments with the pan-PP2A inhibitor okadaic acid at a concentration of 1 nM were performed. At this concentration, the inhibitor is highly selective for PP2A, whereas at higher concentrations, other phosphatases are blocked as well (24). Okadaic acid reduced nuclear phosphatase activity in Nox4$^{-/-}$ cells to the level observed in WT cells (Fig. 3*C*). In line with this, okadaic acid restored the level of γH2AX in Nox4$^{-/-}$ cells to the level of WT cells but had no effect on γH2AX level in WT cells (Fig. 3*D*). Strikingly, low concentration of H_2O_2 that mimics Nox4 activity, restored γH2AX and reduced nuclear PP2A in Nox4$^{-/-}$ cells to the level of WT cells (Fig. 3 *E* and *F*). Collectively, these observations suggest that Nox4-derived H_2O_2 facilitates accumulation of PP2A in the cytosol. In the absence of Nox4, and thus lack of H_2O_2, PP2A accumulates in the nucleus, where it dephosphorylates γ2HAX. Consequently, absence of Nox4 attenuates DNA damage response and promotes genomic instability.

Nox4 Deficiency Retains PP2A in the Cytosol where It Interacts with and Dephosphorylates AKT. Given the sophisticated regulation of PP2A enzyme complexes and their numerous targets, literature mining was performed to obtain a plausible candidate mechanism. Out of several cytosolic proteins promoting tumor survival, the family of AKT kinases is of outstanding importance (25). AKT is highly abundant in tumors (26) and PP2A family members are responsible for the dephosphorylation of AKT (27, 28). Importantly, in a very different context it was suggested that oxidation of AKT can promote its interaction with PP2A (29). On this basis, we speculated that cytosolic interaction of PP2A and oxidized AKT could cause the reduced nuclear localization

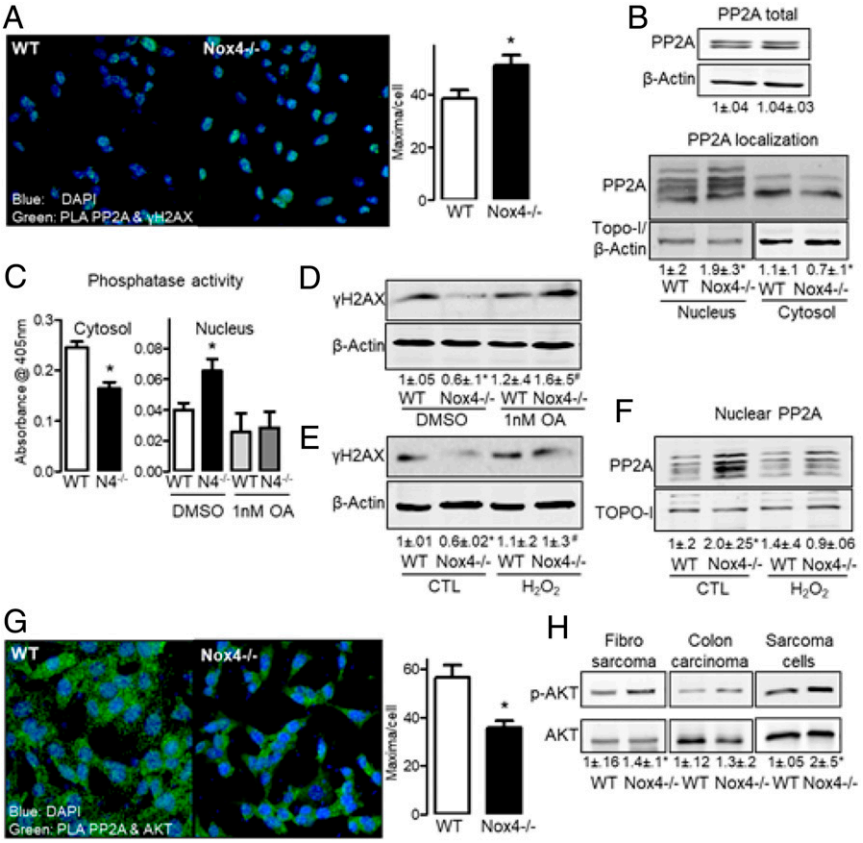

Fig. 3. Nox4 deficiency enhances nuclear PP2A activity, this decreases nuclear γH2AX but increases cytosolic AKT phosphorylation. (*A*) Interaction between PP2A and γH2AX as determined by proximity ligation assay. Quantification of colocalization relative to the number of cells stained with DAPI in %. (*B*) PP2A abundance in cytosolic and nucleus fraction as evaluated by Western blot. (*C*) Serine-threonine phosphatase activity as measured under basal conditions and after treatment with OA in cytosol and nucleus with the aid of NPP as an artificial substrate. (*D* and *E*) γH2AX abundance as quantified by immunoblotting with and without 1 nM of the PP2A inhibitor OA overnight (*D*) or H_2O_2 (24 h, 5 μM (*E*). (*F*) Nuclear expression of PP2A after treatment with or without H_2O_2 as determined by Western blot. All experiments were carried out in isolated fibrosarcoma cells (*F*). Statistics are represented as numbers below the representative Western blots; $^*P < 0.05$ WT vs. Nox4$^{-/-}$, $^{\#}P < 0.05$ Nox4$^{-/-}$ CTL vs. Nox4$^{-/-}$ OA/H_2O_2, $n = 5$. (*G*) Interaction between AKT and PP2A as determined by PLA. Quantification of colocalization relative to the number of cells stained with DAPI in % (*H*). Western blot for phosphorylation of AKT at Ser473 in fibrosarcoma tissue, colon carcinoma tissue, and isolated fibrosarcoma cells of WT and Nox4 $^{-/-}$ mice.

of PP2A. If this hypothesis was correct, nuclear translocation of PP2A in the absence of Nox4 should result in a decreased association of PP2A with its target AKT, and this was what we found (Fig. 3*G*). As PP2A dephosphorylates AKT, the reduced association of AKT and PP2A leaves more AKT phosphorylated in tumor tissue and isolated cells (Fig. 3*H*). Importantly, no evidence for additional phosphorylation of AKT was found. Oxidation, expression, and activity of inducers of AKT phosphorylation such as PTEN or PIP3 were normal (*SI Appendix*, Figs. S8 and S9). We conclude that in the absence of Nox4, PP2A and AKT associate less effectively, which results in lower AKT dephosphorylation and enhanced nuclear translocation of PP2A.

AKT Is a Redox Target of Nox4. The findings described above render the possibility that Nox4 directly promotes the association of AKT and PP2A. Given that the only known function of Nox4 is to produce H_2O_2, redox alterations were likely to be the underlying mechanism. Redox-BIAM switch assays were performed in order to visualize oxidation of AKT. Indeed, loss of Nox4 resulted in a significant reduction of AKT oxidation (Fig. 4*A*). A targeted redox-proteomics approach did not yield sufficient coverage of the peptide sequence of AKT isolated from tissues. Therefore, redox-active cysteines of AKT were mapped from recombinant protein. In a first step, all redox sites of the recombinant AKT were reduced, followed by incubation with H_2O_2. This redox stimulation forced disulfide bridge formations between cysteine 60 and 77 and between cysteine 296 and 310, the latter being conserved in all AKT homologs (Fig. 4*B* and *SI Appendix*, Fig. S10 and Tables S1 and S2). We conclude that Nox4-dependent H_2O_2 formation changes the confirmation of AKT by altering disulfide bridge formation. Accordingly, AKT may provide a redox switch responsible for PP2A translocation.

Oxidized AKT Interacts with the PPP2R1A Scaffolding Subunit of PP2A. The redox nature of the interaction of PP2A and AKT was then analyzed in more detail. Immunoprecipitation of AKT followed by proteomics analysis revealed that PPP2R1A coprecipitates with AKT (Fig. 4*C* and *SI Appendix*, Table S3). PPP2R1A, also known as PP2A subunit A R1α isoform or PR65α, is a scaffolding molecule that coordinates, besides many others, assembly of the catalytic C subunit and the variable regulatory B subunit (30). Potentially, due to detergent conditions optimized for specificity, the PP2A protein complex was disrupted and neither the B nor the C subunit were detected in that approach. Therefore, regular coimmunoprecipitation experiments followed by Western blots with

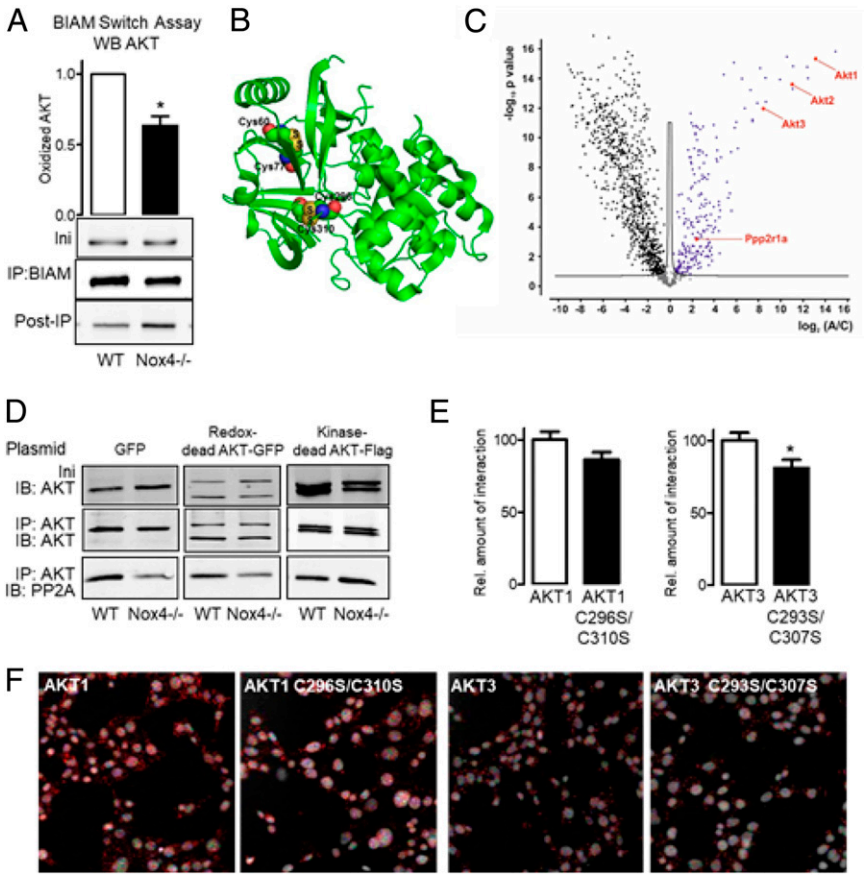

Fig. 4. The interaction of PP2A and AKT is redox sensitive. (*A*) AKT redox modification as analyzed by BIAM switch assay in fibrosarcoma cells of WT and Nox4$^{-/-}$ ($n = 3$). (*B*) Mapping of the H_2O_2-dependently formed disulfide bridges on the structure of human AKT1 as obtained from 4EJN (25) (*SI Appendix*, Tables S1 and S2). (*C*) AKT1 to 3 proteins were immune-captured and copurified interacting proteins were identified by LC/MS. Label-free quantification (LFQ) values were statistically analyzed using permutation test (FDR <0.05, 250 randomizations) (*SI Appendix*, Table S3). Blue and red dots represent significantly enriched proteins. Black and gray dots were enriched in negative control or background, respectively. Marked protein Ppp2r1a was found to be significantly enriched in AKT1 to 3 pull-down samples. (*D*) Coimmunoprecipitation of AKT followed by Western blotting for PP2A catalytic subunit after overexpression with GFP, the redox-dead mutants for AKT1 to 3 and phospho-dead AKT1 mutant. (*E* and *F*) Proximity ligation in wild-type fibrosarcoma cells after overexpression of AKT1 and AKT3 and AKT1 and AKT3 redox-dead mutants (*F*). Antibodies used for AKT1 were PP2A and HA and for AKT3 PP2A and GFP. Red indicates dots of proximity, while gray represents DAPI staining of nuclei. Results of cells overexpressed with wild-type AKT were set to 100% (*E*). *$P < 0.05$ was considered significant.

an antibody directed against both C subunits of PP2A (31) were performed. These experiments demonstrated an interaction of PP2A subunit C with AKT in WT cells, which was impaired in Nox4$^{-/-}$ cells (Fig. 4*D*). Overexpression of a kinase-dead mutant (T308A/S473A) rescued coprecipitation of PP2A and AKT to the level observed in wild-type cells (Fig. 4*D*). In contrast, overexpression of redox-dead mutants of AKT did not restore coprecipitation of AKT and PP2A. Accordingly, PLAs demonstrated an attenuated interaction of redox-dead AKT mutants with PP2A even in WT cells (Fig. 4 *E* and *F*). Collectively, these data suggest an interaction of PP2A and AKT, potentially via PPP2R1A, which requires Nox4-dependent oxidation, but no kinase function of AKT.

Kinase- but Not Redox-Dead AKT Restores Normal Cell Function in Nox4$^{-/-}$ Cells. In order to verify the in vivo relevance of our findings, subcellular distribution of PP2A as a consequence of AKT oxidation was analyzed. In Nox4 knockout cells, overexpression of any of the three wild-type AKT homologs or kinase-dead versions of AKT restored cytosolic retention of PP2A to the level observed in wild-type cells. In contrast, the redox-dead cysteine mutant of AKT did not have the same effect (Fig. 5*A*). Consequently, nuclear accumulation of PP2A was reduced upon overexpression of all but the redox-dead AKT (Fig. 5*B*). According to our model, restoration of the cytosolic level of PP2A should restore DNA damage detection and thus phosphorylation of H2AX. Indeed, overexpression of wild-type AKT restored γH2AX in Nox4$^{-/-}$ cells to the level observed in WT cells. In contrast, overexpression of redox-dead AKT failed to have this effect (*SI Appendix*, Fig. S11). As a consequence of PP2As cytosolic disposition, overexpression of all but the redox-dead AKT mutants should promote DNA repair. To address this, comet assays were performed in cells overexpressing the different AKT plasmids. Wild-type AKT reduced the number of comets in Nox4$^{-/-}$ cells to the level of WT cells and similar effects were observed in cells overexpressing kinase-dead mutants of AKT (Fig. 5 *C* and *D*). In contrast, none of the redox-dead versions of AKT was able to reduce the number of comets. Thus, cytosolic retention of PP2A due to its association with Nox4-oxidized AKT stabilized γH2AX in the nucleus, which affords an appropriate DNA damage repair.

Discussion

This study provides evidence for genomic instability as a consequence of genetic deletion of the NADPH oxidase Nox4. Nox4 provides a basal tone of H_2O_2, which oxidizes AKT. Oxidized AKT binds to PP2A and subsequently sequesters this phosphatase in the cytosol. In the absence of Nox4, none-oxidized AKT does not bind PP2A. The phosphatase then translocates into the nucleus and dephosphorylates γH2AX, a main component of DNA damage recognition and repair. Consequently, due to poor recognition, DNA damage remains unrepaired and accumulates to a level higher than normal. Unrecognized DNA damage prevents expression of tumor suppressors such as p53, even upon exposure to DNA damaging cancerogens. Eventually, cancerogens can lead to enhanced tumor formation in Nox4$^{-/-}$ mice.

The role of ROS is ambivalent and especially in diseases like cancer, ROS can have beneficial and harmful effects. ROS activate cancer-associated fibroblasts and on the other hand force apoptosis of damaged cells, for example. A recent review is recommended for further reading (32). Endogenous ROS generator systems, like the NADPH oxidase family, produce ROS in a controlled and inducible manner. Via thiol-based systems those ROS then mediate signal transduction (33). Nox4 is the only member of the NADPH oxidase family that constitutively produces H_2O_2. Thereby Nox4 provides a basal oxidative tone to the cell, which is protective by preventing inflammation (11) and maintaining the activity of antioxidant systems like KEAP/Nrf2 (12, 34) and protein kinase A (35, 36).

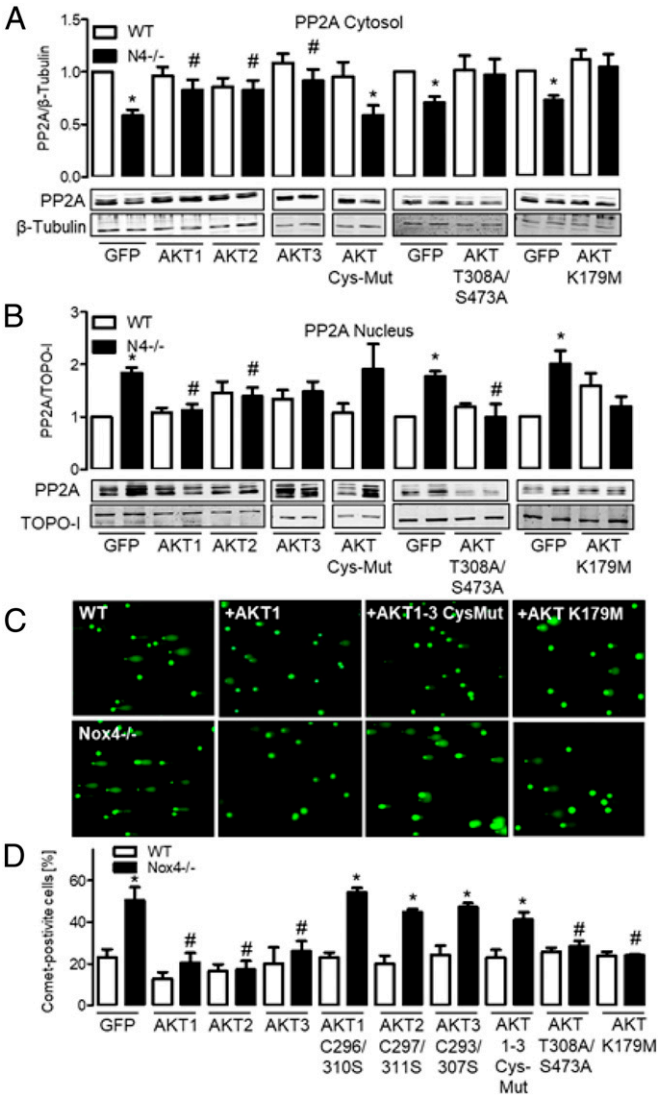

Fig. 5. PP2A translocation can be rescued by overexpressing AKT. PP2A (catalytic subunit) localization in the cytosol (*A*) and nucleus (*B*) was determined by Western blot after nuclear extraction. Cells were overexpressed with the plasmids indicated. *$P < 0.05$; WT/WT mutated AKT vs. Nox4$^{-/-}$/Nox4$^{-/-}$ mutated AKT, $^{\#}P < 0.05$ Nox4$^{-/-}$ vs. Nox4$^{-/-}$ AKT OE, $n = 5$). (*C*) Comet assay, exemplary photos (*C*) and statistics (*D*) of WT and Nox4$^{-/-}$ cells with overexpression of the plasmids indicated *$P < 0.05$ WT vs. Nox4$^{-/-}$, $^{\#}P <$ 0.05 Nox4 GFP vs. Nox4$^{-/-}$ AKT mutant. $n = 5$.

The present work establishes AKT as an additional redox target of Nox4. Oxidation of AKT by Nox4 promoted the interaction of PP2A with AKT, which facilitated AKT dephosphorylation. Accordingly, AKT phosphorylation and potentially its activity rises in the absence of Nox4. Given that AKT promotes survival and proliferation, this finding explains faster proliferation after deletion of Nox4, observed not only in this but also other studies (37). In several tumor cell lines, Nox4 was identified to drive AKT phosphorylation (19, 38–41), while other studies identified AKT as an inducer of Nox4 expression (42–45). These conflicting results are potentially based on unspecific effects of ROS and their random association with Nox4 expression. In fact, any reduction of ROS, like inhibition of mitochondria, Nox1, Nox2, or Nox4, usually leads to a similar protective response in transformed stable tumor cell lines (46–48).

A secondary effect of AKT oxidation by Nox4 and subsequent binding of PP2A to AKT is to deprive other cellular compartments from the phosphatase. After Nox4 knockout AKT is less oxidized, PP2A is released from AKT and translocates into the nucleus, where it dephosphorylates γH2AX (22). γH2AX is H2A, phosphorylated by ATM at Ser139, an effect occurring at sites of DNA double-strand breaks (49) which represents a major prerequisite for a cell's response to DNA damage (23). The present observation of less γH2AX in the absence of Nox4 verifies a previous report where antioxidants reduced the level of γH2AX in murine lung cancer tumors (5).

Phosphatases themselves are well-known redox switches as well. Dual-specific phosphatases like the lipid phosphatase PTEN and tyrosine phosphatases (PTPs) are inactivated by H_2O_2. Nox1 inactivates PTEN (50) and inhibition of Nox1 induces apoptosis by attenuating AKT signaling in cancer cells (51). PTP inactivation by Nox4-derived H_2O_2 occurs under certain conditions and promotes survival of some cancer cells (47, 52). However, in most cells the tonic activity of Nox4, induces antioxidant defense mechanisms to counteract this process (34, 53, 54). PP2A, the phosphatase of concern in the present work, does not contain a redox-sensitive cysteine but a metal in its active center (55). Therefore, PP2A is not a direct target of Nox4-derived H_2O_2. Apart from that, PP2A was thought to be a tumor suppressor as okadaic acid and other PP2A inhibitors can serve as carcinogens (56). In contrast, inactivation of PP2A triggers tumor-selective cell death (57) and the PP2A inhibitors cantharidin or okadaic acid induce apoptosis of pancreatic cancer cells through persistent phosphorylation of IKKα and a sustained activation of NFκB (58). Subcellular localization of PP2A activity may be the key to understand the controversial findings. The B subunit determines function and localization of its PP2A complex. In fact, if not retained in the cytosol, a B56ε containing PP2A holoenzyme has been described to dephosphorylate γH2AX (59).

Limitations of the Study. The role of ROS in cancer is complex, and may vary between different types of cancer, and certainly varies at different stages of tumor initiation, development, and progression (60). This is likely to be the case for Nox4 as well. No evidence for development of spontaneous tumors in Nox4$^{-/-}$ mice was found so far. Accordingly, based on the data presented, Nox4 may not play a role in tumor initiation or progression. Rather the two-hit model of cancer initiation suggests a role for Nox4 in tumor development only in the presence of an applied cancerogen.

Several studies report increased expression of Nox4 in cancer (40, 61). Indeed, Nox4 is induced by hypoxia and fibrotic response, both of which are common in tumors. Thus, induction of Nox4 is unlikely to cause tumor formation, but rather represents a cellular defense mechanism due to altered homeostasis and cytokine microenvironment in a growing tumor. Indeed, some studies suggest a protective effect of Nox4 in cancer. A silenced Nox4 promoter promotes hepatocarcinogenesis in rats (62); and in human hepatocellular carcinoma, high Nox1 expression was associated with less favorable outcome, whereas high Nox4 expression was beneficial (63, 64). In a more descriptive study Nox4 siRNA prevented liver cancer in a xenograft model (65). In head and neck cancer cells an inhibitor of epidermal growth factor receptor induced autophagy in a Nox4-dependent way (66). These data underline the ambivalent role of Nox4 in cancer.

Lastly, different to our results, other studies linked NADPH oxidases to an increase in DNA damage. Up-regulation of p22phox contributes to genomic instability in FLT3-expressing leukemia cells (67) and H-Ras transformed cell lines are protected from DNA damage if treated with Nox4 siRNA (68). Additionally Nox1 was associated with DNA damage in cell lines (69). These variable results stress that tumor research on cell lines should be interpreted with caution. Cultured cells often present with overwhelming ROS formation that indeed harms the cells. The selection above, however, illustrates an interchangeability of individual Nox enzymes, which may not reflect the in vivo situation.

Conclusion

The current work establishes Nox4 as an endogenous source of ROS that maintains genomic stability. This work supports and partially explains clinical data showing that antioxidants do not protect from cancer and may even be harmful under certain conditions. We hope our work will strengthen the acknowledgment of the pleiotropic and contextual actions of ROS and NADPH oxidases in cancer and most other diseases.

Materials and Methods

Materials. The following chemicals were used: MCA, AOM, NaCl, NH_4Cl, $NaHCO_3$ Hanks' BSS without Ca^{2+} and Mg^{2+} and trypsin-EDTA solution (T3924) from Sigma-Aldrich, DSS (16011080; MP Biomedicals), Dulbecco's PBS (GIBCO), Hanks' buffer, SYBR green and Na-EDTA from Applichem, Tris (Carl Roth), and fibronectin (Corning). Collagenase type 2 was purchased from Worthington. The PI3-kinase inhibitor Ly294002 (BML-ST420) was acquired from Enzo Life Science. The following antibodies were used: anti-pH3 (06-570), anti-PP2A, and anti-phospho-histone H2A.X (Ser139) from Millipore, anti-AKT, anti-phospho-AKT (Ser473), p-p53 (Ser15), ATM, HA, and PTEN, Erk, p-Erk, AKT Sepharose bead conjugate and IgG mouse Sepharose bead conjugate from Cell Signaling, anti-p53 (FL-393), anti-p110, NQO1, p-ATM (Ser1981), GFP and anti-topoisomerase 1 (C-15) from Santa Cruz, anti-β-actin (AC-15) from Sigma-Aldrich, and anti-p85 from BD Transduction Laboratories. Fluorogenic substrates for proteasome activity were purchased from Boston Biochem. Human recombinant AKT1 (ab116412) was purchased from Abcam.

Animals and Animal Procedures. All animal experiments were approved by the local governmental authorities (approval nos. F28/27, F28/46, FU\1194, and FU\1235) and performed in accordance with the animal protection guidelines. Nox1y/– mice, kindly provided by Karl-Heinz Krause, University of Geneva, and previously characterized, were used for the same experiments (70). C57BL/6J and Nox2y/– mice were purchased from Charles River. Nox4$^{-/-}$ mice were generated by targeted deletion of the translation initiation site and of exons 1 and 2 of the Nox4 gene (11), backcrossed into C57BL/6J for more than 10 generations. Tamoxifen-inducible Nox4$^{-/-}$ mice (Nox4flox/flox-ERT2-Cre+/0 mice) were produced by crossing Nox4flox/flox mice (backcrossed more than 10 generations into C57BL/6J) with Cre-ERT2+/0 mice (11). Genetic deletion of Nox4 in Nox4flox/flox-ERT2-Cre+/0 mice was achieved by oral tamoxifen administration in the chow (LASCRdiet CreActive TAM400, LASvendi) for 10 consecutive days at the age of 7 wk. Both Cre-positive as well as Cre-negative littermates received tamoxifen. For generation of fibroblast-specific Nox4flox/flox_Col1a2-CreERT2 mice, Col1a2-CreERT2 (Stock No. 029235 Tg(Col1a2-cre/ERT,-ALPP)7Cpd/J; The Jackson Laboratory) were crossed with Nox4flox/flox mice. For generation of the enterocyte-specific Nox4flox/flox_Villin-CreERT2 Nox4flox/flox were in vitro fertilized with sperm from Villin-CreERT2 mice (71). Validation of the cell-specific knockout was performed (*SI Appendix*, Fig. S12) as well as analysis of Nox4 in organoids, colon tissue, and tumors (*SI Appendix*, Fig. S13).

Mice were housed in a specified pathogen-free facility with 12/12 h day and night cycle and free access to water and chow every time. If not stated differently, tumor induction in constitutive knockouts and littermates started when the mice reached an age of 7 to 8 wk. In the case of tamoxifen-inducible knockout, tamoxifen administration started at the age of 7 wk, followed by tumor initiation. Fibrosarcoma induction was achieved by subcutaneous injection of the chemical carcinogen MCA into the right flank of the mice. In the cases that tumors reached a diameter of 1.5 cm or 150 d after MCA injection, mice were killed and if present the tumor tissue was used for cell isolation and immunohistological and biochemical analysis. In order to analyze short-term effects of MCA injection, mice were killed 20 d after MCA injection and skin at the site of injection was used for histological and biochemical analysis. Colon carcinomas were induced by the following procedure: A single intraperitoneal dose of 10 mg/kg body weight AOM was applied. After 1 wk, drinking water was supplemented with 1.5 or 2% DSS for 1 wk followed by 2 wk of usual drinking water. This procedure was

repeated two more times. Two weeks after the third DSS cycle, mice were killed and colons were used for further analysis.

Cell Culture. Fibrosarcoma cells were isolated using the tumor dissociation kit for mouse and the gentle MACS Dissociator from Miltenyi Biotec, following the manufacturer's instructions. In brief, tumor tissue was homogenized enzymatically, erythrocytes were lysed, and eventually cells were cultured in Dulbecco's modified Eagle's medium (DMEM) + glutaMAX (GIBCO) supplemented with 5% fetal calf serum (FCS) and 1% penicillin (Pen) (50 U/mL) and streptomycin (Strep) (50 μg/mL) in a humidified atmosphere of 5% CO_2 at 37 °C. Erythrocyte depletion buffer contained 155 mM NH_4Cl, 10 nM $NaHCO_3$, and 100 nM EDTA in double distilled water, with a pH = 7.4.

For isolation of dermal skin fibroblasts from mice 1 cm^2 piece of skin was cut into small pieces, transferred into 2.5 mL collagenase solution (1,000 U/mL in Hanks' without Ca^{2+}/Mg^{2+}) and incubated on a shaker for 105 min at 37 °C. Afterward the solution was resuspended and transferred through a 70-μm nylon filter. Cells were centrifuged and placed on a fibronectin-coated dish. Primary fibroblasts were cultured in DMEM/F-12 (GIBCO, Life Technologies) supplemented with 10% FCS and 1% Pen/Strep in a humidified atmosphere of 5% CO_2 at 37 °C. Murine lung endothelial cells were isolated and cultured as described by Schröder et al. (11). Crypt isolation and organoid cultures from murine intestine were achieved as described (72), using the Intesticult System from StemCell Technologies according to manufacturer's instructions. Additionally, 100 ng/mL murine Wnt3a (Peprotech) was added to the medium. A total of 700 crypts were seeded in 50 μL mixture of Matrigel and Intesticult medium in 24-well plates. A total of 400 μL of medium per well was used. Organoids were analyzed by light microscopy and qRT-PCR.

Analysis of the Redox State of Isolated Fibroblasts. In order to analyze for the redox state of the isolated cells, we utilized the GSH/GSSG-GloTM assay (Promega). We followed the manual provided by the manufacturer: cells were lysed with passive lysis buffer or oxidized gluthathione lysis reagent that contain luciferin-NT, the luminogenic GSH probe required for the assay chemistry. After addition of luciferin and incubation for 15 min, luminescence was measured and GSH as well as GSSG were calculated with the aid of a standard curve.

Dihydroethidium (DHE) assays in an HPLC setting was performed as described before (73). Dihydroethidium (DHE, 20 μmol/L) was oxidized by the cells and the resulting products 2-dihydroxyethidium (2EOH) and ethidium (E) from cells and supernatant were separated by HPLC and analyzed by absorbance (350 to 400 nm for DHE) and fluorescence (510 nm/595 nm excitation/emission for 2EOH and E). For fluorescence detection, DHE and its oxidation products were separated by HPLC (Hitachi, Elite Lachrom System L3130 pump) using a C18 column (EC, Nucleosil, 100-5, 250/4.6 Macherey Nagel), a mobile phase A of H_2O:acetonitrile:trifluoroacetic acid (TFA) (9:1:0.1) and phase B of acetonitrile +0.1% TFA. A gradient from 0 to 40% of phase B was achieved within 10 min and to 100% phase B in 20 min with a 0.5 mL/min flow. To estimate 2EOH concentration, potassium superoxide (14 mmol/L) was used as a standard. System control and analytical data analysis were processed by Analyst software 1.6.2.

For Amplex Red measurement, cells were incubated in PBS containing 100 μm Amplex Red and 0.25 units/mL horse radish peroxidase (HRP) (Thermo Fisher). After 30 min, the supernatant was transferred to a 96-well plate, and fluorescence of resorufin as the product of H_2O_2-dependent oxidation of Amplex Red was measured in a microplate fluorimeter (excitation 540 nm, emission 580 nm).

Site-Directed Mutagenesis and Transfection of Plasmids. The QuikChange II XL Site-Directed Mutagenesis Kit (200521, Agilent) was used to insert point mutations into AKT1/2/3. Corresponding primers were designed with the QuikChange Primer Design Program. Plasmids for mouse AKT1 (39531), AKT2 (64832), and AKT3 (27293) from Addgene were used for converting the two cysteine residues of AKT into serine. The following primers were used for the introduction of single amino acid mutations: AKT1 C296S 5′-ATC CCC TCC TTG CTC AGC CCG AAG TCC-3′ and 5′-GGA CTT CGG GCT GAG CAA GGA GGG GAT-3′; AKT1 C310S 5′-CTC CGG CGT TCC GCT GAA TGT CTT CAT AGT GGC-3′ and 5′-GCC ACT ATG AAG ACA TTC AGC GGA ACG CCG GAG-3′; AKT2 C297S 5′-CTG ATG CCC TCT TTG CTC AAG CCA AAG TCA GTG-3′ and 5′-CAC TGA CTT TGG CTT GAG CAA AGA GGG CAT CAG-3′; AKT2 C311S 5′-TAC TCC GGG GTA CCA CTG AAG GTT TTC ATG GTG-3′ and 5′-CAC CAT GAA AAC CTT CAG TGG TAC CCC GGA GTA-3′; AKT3 C293 S 5′-CTG TGA TCC CTT CTT TGC TAA GCC CAA AAT CCG TAA TTT TT-3′ and 5′-AAA AAT TAC GGA TTT TGG GCT TAG CAA AGA AGG GAT CAC AG-3′; AKT3 C307S 5′-GTA CTC TGG TGT GCC ACT GAA TGT CTT CAT GGT AG-3′ and 5′-TAC CCA TGA AGA CAT TCA GTG GCA CAC CAG AGT AC-3′. Double mutants (C296/310, C297/311, and C293/307) were constructed using single mutants as DNA template and primers for C310S/C311S/C307S. Experiments were performed according to the manufacturer's protocol and mutations were verified by sequencing. Kinase-dead AKT1 S473A/T308A mutant was a gift from Itamar Goren, Institute of Pharmacology, University of Frankfurt, Germany, and catalytically inactive AKT K179M from Beate Fisslthaler, Institute for Vascular Signaling, University of Frankfurt, Germany. Lipofectamine 3000 (L3000-015) was used for transfection of basal AKT plasmids and mutants according to the manufacturer's instructions.

Proximity Ligation Assay. Proximity ligation assay allows the direct detection of protein interactions with high specificity and sensitivity with the aid of two specific antibodies for the proteins of interest. Analysis was performed as described in the manufacturer's protocol (Duolink II Fluorescence, OLink). Briefly, isolated fibrosarcoma cells were fixed in phosphate buffered formaldehyde solution (4%), permeabilized with Triton X-100 (0.2%), blocked with serum albumin solution (3%) in phosphate buffered saline, and incubated overnight with appropriate antibodies. After washing, samples were incubated with the respective PLA probes for 1 h, washed, and ligated for 30 min, both at 37 °C. An additional washing step followed and amplification with polymerase was performed for 100 min. Images were obtained by confocal microscopy with an LSM 510 (Zeiss). Fiji software was used for quantification of single dots per cell.

Protein and Western Blot Analysis. For whole cell protein isolation, cells were lysed in a buffer containing 20 mM Tris/cl pH 7.5, 150 nM NaCl, 10 mM $NaPP_i$, 20 nM NaF, 1% Triton, 10 nM okadaic acid (OA), 2 mM orthovanadat (OV), protein-inhibitor mix (PIM) and 40 μg/mL phenylmethylsulfonyl fluoride (PMSF).

For separation of nucleus and cytosol, the cells were lysed in buffer A (10 nM Hepes pH 7.9, 10 nM KCL, 0.1 mM EDTA, 0.1 mM EGTA, 1% Nonidet, 10 mM DTT, PIM, 40 μg/mL PMSF. Cells were centrifuged to gain the cytosol-containing supernatant. The pellet was further lysed with buffer C (20 mM Hepes pH 7.9, 0.4 M NaCl, 1 mM EDTA, 1 mM EGTA, 10 mM DTT, PIM, 40 μg/mL PMSF) to obtain the nuclear extract. A Bradford assay was used to determine the protein amount (74). Samples were boiled in sample buffer and transferred on SDS-PAGE followed by Western blotting. Identical amounts of protein from nuclear and cytosolic fractions were loaded. Analysis was performed with an infrared-based detection system using fluorescent-dye-conjugated secondary antibodies from LI-COR Biosciences.

Phosphatase activity was analyzed according to the manufacturer's suggestion. Briefly, 50 mM para-nitrophenylphosphate (pNPP) were incubated with lysates of cytosolic or nuclear fractions prepared as described above. After 5 to 10 min the reaction was stopped by addition of NaOH and the amount of the product of the phosphatase reaction, p-nitrophenol, was determined by measuring the absorbance at 405 nm in a microplate reader (Tecan Infinite 200 Pro).

BIAM switch assay was performed to determine the oxidation state of AKT. Briefly, cells were blocked with n-ethylmaleimide (NEM) and scraped in trichloroacetic acid (TCA). To block the free thiols, cell pellets were resuspended in NEM-denaturing buffer (containing Tris·HCl pH 8.5, urea, EDTA, and SDS) subsequently followed by acetone precipitation. Reduction of oxidized thiols was performed with DTT-denaturing buffer and labeling of those with biotin-polyethyleneoxide-iodoacetamide-denaturing buffer followed by acetone precipitation and Triton lysis. Lysates were used for immunoprecipitation (IP) with streptavidin-agarose beads and blotted for AKT.

mRNA Isolation and RT-qPCR. Total mRNA from cells and frozen homogenized tissue was isolated with a RNA-Minikit (Bio-Sell) according to the manufacturer's protocol. Random hexamer primers (Promega) and SuperScript III Reverse Transcriptase (Invitrogen) were used for cDNA synthesis. Semiquantitative real-time PCR was performed with a Mx3000P qPCR cycler (Agilent Technologies) using PCR Eva Green qPCR Mix with ROX (Bio-Sell) with appropriate primers. Relative expression of target genes was normalized to eukaryotic translation elongation factor 2 (EF2), analyzed by the delta-delta-Ct method, and given as percentage compared with control experiments. Primer sequences for murine Nox4 were forward 5′-TGTTGG-GCCTAGGATTGTGTT-3′ and reverse 5′-AGGGACCTTCTGTGATCCTCG-3′. For p53 forward 5′-AGACCGCCGTACAGAAGAAG3′ and reverse 5′-TTCAGCTCC-CGGAACATCTC-3′, Cyp1A1 forward 5′-GGCCACTTTGACCCTTACAA-3′ and reverse 5′-CAGGTAACGGAGGACAGGAA-3′ -3′, for Cyp1B1 forward 5′-TTC-TCCAGCTTTTTGCCTGT-3′ and reverse 5′-TAATGAAGCCGTCCTTGTCC-3′, and ATM forward 5′-ATGCCAGTCTTTTCAGGGTG-3′ and reverse 5′-TCAGAAGCT-GGGAGTGCTTC-3′.

DNA Damage Detection (Comet and Nicoletti Assays). A suspension of 1×10^6 cells/mL was mixed 1:10 with 5% low melting agarose and subjected onto slides coated with 1.5% normal melting agarose. Lysis of the cells was performed for 2 h at 4 °C in lysis buffer (2.5 M NaCl, 10 mM Tris, 100 mM EDTA, pH = 10, 1% Triton X-100, and 10% SDS in double distilled water). Lysis was followed by a 20-min incubation of the slides on ice with the alkaline electrophoresis buffer (300 mM NaOH and 0.5 M EDTA) with subsequent electrophoresis at 25 V for 20 min. Slides were washed three times with PBS and stained with SYBR green. Pictures were taken with confocal microscope LSM 510 Meta and quantification was performed manually by three independent investigators determining the ratio of cell number/cells with comets.

Additionally DNA fragmentation was determined by analysis of propidium iodide (PI)-stained nuclei using flow cytometry as described previously (75). Cells were lysed and stained for 2 h in a solution of 0.1% trisodium citrate dehydrate and 0.1% Triton X-100 containing 50 μg/mL propidium iodide (Sigma) and analyzed by flow cytometry (FACSCanto II, BD Biosciences).

Immunohistochemistry. Tissue was fixed in 4% paraformaldehyde overnight, dehydrated in ascending ethanol series, and then embedded in paraffin. Paraffin blocks were sliced and slides were dewaxed for further staining in descending ethanol series from 100 to 70%. For antigen retrieval, slides were cooked 10 min in citrate 1× TRS buffer (target retrieval solution; Dako). After cooling down staining procedure started using the Dako CSA system in combination with biotin blocking system (Dako) for 3,3′ diaminobenzidine staining. First, slides were blocked with avidin and biotin for 20 min with the biotin blocking system from Dako, followed by peroxidase and protein blocking from the Dako staining kit. In between washing steps were performed with TBST (Tris-buffered saline with Tween20). After the protein block, the first antibody was applied on the slides overnight at 4 °C. The next day slides were incubated with biotinylated secondary antibody, amplification steps were performed as described in the manual, and diaminobenzidine was used to generate the signal. Counterstaining was performed with hematoxylin.

RNAscope. In situ hybridization by the RNAscope technique was performed according to the manufacturer's instructions (Advanced Cell Diagnostics). Briefly, 4-μm-thick sections were deparaffinized and treated with H_2O_2, followed by antigen retrieval and protease treatment. Probes for Nox4 (RNAscope LS 2.5 Probe- Mm-Nox4, Cat. No. 457268), and positive/negative controls (peptidylprolyl isomerase B, RNAscope Probe-Mm-Ppib-C4, Cat. No. 313911-C4 (*Bacillus subtilis* dihydrodipicolinate reductase, RNAscope negative control probe-DapB Cat. No. 310043) were used. Probes were hybridized for 2 h followed by six amplification steps. The signal was detected with RNAscope 2.5 HD Reagent Kit-BROWN (Cat. No. 322300) and specimens were counterstained with Gill's hematoxylin No. 1 and visualized with a light microscope.

Polysomal Fractionation. Isolated fibrosarcoma cells were seeded in a 15-cm dish 1 d prior to harvesting. Polysome analysis was performed as described previously (76). Briefly, after incubation with 100 μg/mL cycloheximide for 10 min at 37 °C, cells were scraped and centrifuged. The supernatant was discarded, pellet washed, centrifuged again, and lysed in 750 μL polysome buffer (140 mM KCl, 20 mM Tris·HCl pH 8.0, 5 mM MgCl2, 0.5% Nonidet P-40, 0.5 mg/mL heparin, 1 mM DTT, 100 U/mL RNasin [Promega], 100 μg/mL chlorhexidin). After centrifugation for 5 min, 16,000 rpm at 4 °C and transferring the supernatant into a fresh tube, 600 μL of cytoplasmic lysate was layered onto a 10- to 50% continuous sucrose gradient. The gradient was centrifuged at 35,000 rpm for 2 h without braking, and the gradients were collected in 1-mL fractions using a gradient station (Biocomp). Absorbance was measured at 254 nm. RNA was precipitated by addition of sodium acetate (3 M) and isopropanol. RNA was further purified using the Nucleospin RNA Kit (Macherey-Nagel) according to the manufacturer's manual and analyzed by RT-qPCR.

Mass Spectrometry Measurements of Inositol Lipids. Mass spectrometry was used to measure inositol lipid levels essentially as described previously (77) using a QTRAP 4000 (AB Sciex) mass spectrometer and employing the lipid extraction and derivatization method described for cultured cells (cells isolated from tumors) and whole tissue (tumor tissue), with the modification that initial samples were probe sonicated for 5 seconds (using a microtip) prior to extraction and that final samples were dried in a speedvac concentrator rather than under N2. Measurements were conducted on 1×10^6 isolated fibrosarcoma cells or 1 mg wet weight tumor tissue per sample. C16:0/C17:0 PI (100 ng) and PIP3 (10 ng) internal standards (ISDs) were added to each sample prior to extraction. Integrated area of lipid species peaks were corrected for recovery against ISD area (giving a response ratio for each lipid) and data expressed as C18:0 C20:4 PIP3 response ratio normalized to C18:0 C20:4 PI response ratio to account for cell input variation. Both endogenous PIP3 and PI were corrected to their own internal standard, and then the one measurement was divided by the other, to get the best estimate of true PIP3/PI.

Sample Preparation and Mass Spectrometry. A total of 2.5 μM recombinant AKT1 (Abcam) was reduced in 100 μM DTT and treated with 300 μM H_2O_2 for 30 min. Proteins were directly digested overnight with trypsin (sequencing grade, Promega) and analyzed by liquid chromatography/mass spectrometry (LC/MS).

Fibrosarcoma cells of wild-type and Nox4-deficient mice were lysed in buffer A. Lysates were used to trap AKT1 to 3 including interacting proteins using a Sepharose beads immobilized AKT antibody and IgG (Cell Signaling) as negative control. Beads were washed in PBS, resuspended in 50 μL 8 M urea, 50 mM Tris/HCl, pH 8.5, and incubated at 22 °C for 30 min. Thiols were alkylated with 40 mM chloroacetamid and samples were diluted with 25 mM Tris/HCl, pH 8.5, 10% acetonitrile to obtain a final urea concentration of 2 M. Proteins were digested with 1 μg trypsin/LysC (sequencing grade, Promega) overnight at 22 °C under gentle agitation. Digestion was stopped by adding trifluoroacetic acid to a final concentration of 0.1%. Peptides were loaded and purified on multistop-and-go tip (StageTip) containing six C18 disks (78). Peptides were dried and resolved in 1% acetonitrile, 0.1% formic acid, and analyzed by LC/MS.

LC/MS was performed on a Thermo Scientific Q Exactive Plus equipped with an ultra-high performance liquid chromatography unit (Thermo Scientific Dionex Ultimate 3000) and a Nanospray Flex Ion-Source (Thermo Scientific). Peptides were loaded on a C18 reversed-phase precolumn (Thermo Scientific) followed by separation on a 2.4 μm Reprosil C18 resin (Dr. Maisch GmbH) in-house packed picotip emitter tip (diameter 100 μm, 15 cm long, New Objectives) using a gradient from mobile phase A (4% acetonitrile, 0.1% formic acid) to 30% mobile phase B (80% acetonitrile, 0.1% formic acid) for 20 min (purified human AKT1) or 90 min (AKT1 enriched from lysate) followed by a second gradient to 60% B for 10 min or 15 min, respectively. MS data were recorded by the data-dependent acquisition Top10 method selecting the most abundant precursor ions in positive mode for HCD (higher-energy collisional dissociation) fragmentation. The full MS scan range was 300 to 2,000 *m/z* with resolution of 70,000, and an automatic gain control (AGC) value of 3×10^6 total ion counts with a maximal ion injection time of 160 ms. MS/MS scans were recorded with a resolution of 17,500, an isolation window of 2 *m/z*, and an AGC value set to 10^5 ions with a maximal ion injection time of 150 ms. Selected ions were excluded in a time frame of 30 s following the fragmentation event.

Data analysis of purified human AKT1: Xcalibur raw files were analyzed by Peaks7 Studio software for proteomics (http://www.bioinfor.com/; Bioinformatics Solutions). The enzyme specificity was set to trypsin. Missed cleavages were limited to 3. Monoisotopic precursor mass error tolerance was 5 ppm, and fragment ion tolerance was 0.05 Da. The following variable modifications were selected: of methionine (+15.99), disulfide bridge (−2.02), half of disulfide bridge (−1.01), dioxidation on cysteines (+31.99), and trioxidation on cysteines (+47.98). After de novo sequencing of spectra, the human reference proteome set (download from Uniprot, April 4, 2015; 68,511 entries; https://www.uniprot.org/) was used to identify peptide–spectrum matches with a false discovery rate (FDR) of 1%. For identification of cross-linked peptides by disulfide bridges, a special software StavroX (v3.4.12) (79) was used. A disulfide bridge (−2.01565) was included and the search for dipeptides was done using a precise scoring mode. Only dipeptides with the highest scores (>200) were inspected and are shown in *SI Appendix*, Table S2. Disulfide bridges within the structure of AKT1 (4EJN) (80) were illustrated using Pymol (0.99rev9).

Data analysis of immune-trapped AKT1 to 3: Xcalibur raw files were analyzed by MaxQuant (1.5.2.8) (81) with specificity to trypsin and tolerated missed cleavages of 2. The following variable modifications were selected: of methionine (+15.99), carbamidomethylation on cysteines (+57.02), and acetylation on N terminus (+42.01). Proteins were identified using a mouse proteome set (Uniprot, June 26, 2015, 76,086 entries) with a FDR of 1%. Proteins were quantified using label-free quantification (LFQ) with at least one peptide and further analyzed by Perseus 1.5.4.1 (82). Reverse hits, known contaminants, and identified by side proteins were removed from the list. Missing LFQ values were replaced by a background value generated from the normal distribution to enable calculation of ratios to control. A permutation test was performed to identify interacting proteins on AKT1 to 3.

Statistics. All values are mean ± SEM. Statistical analysis was performed by ANOVA followed by LSD (least significant difference) post hoc testing or by *t* test, as appropriate. Tumor-free survival curves were compared by ANOVA for repeated measurements. Densitometry was performed with Odyssey software. A *P* value of less than 0.05 was considered statistically significant.

Data Availability. All study data are included in the article and/or *SI Appendix*.

ACKNOWLEDGMENTS. We are grateful to Manuela Spaeth, Sabine Harenkamp, Maria Walter, and Jana Meisterknecht for their excellent technical support of our study. Furthermore, we thank Itamar Goren and Beate Fisslthaler for providing AKT mutant plasmids. This work was supported by grants from the Deutsche Forschungsgemeinschaft (SCHR1241/1-1 and SFB815/TP1 to K.S., TP8 to B.B., and Z1 to I.W.) and the Fraunhofer Gesellschaft (Graduate School Translational Research Innovation Pharma [TRIP]) to K.S.

1. E. Lonn *et al*.; HOPE and HOPE-TOO Trial Investigators, Effects of long-term vitamin E supplementation on cardiovascular events and cancer: A randomized controlled trial. *JAMA* **293**, 1338–1347 (2005).
2. G. S. Omenn *et al*., Risk factors for lung cancer and for intervention effects in CARET, the beta-carotene and retinol efficacy trial. *J. Natl. Cancer Inst.* **88**, 1550–1559 (1996).
3. Alpha-Tocopherol, Beta Carotene Cancer Prevention Study Group, The effect of vitamin E and beta carotene on the incidence of lung cancer and other cancers in male smokers. *N. Engl. J. Med.* **330**, 1029–1035 (1994).
4. E. A. Klein *et al*., Vitamin E and the risk of prostate cancer: The selenium and vitamin E cancer prevention trial (SELECT). *JAMA* **306**, 1549–1556 (2011).
5. V. I. Sayin *et al*., Antioxidants accelerate lung cancer progression in mice. *Sci. Transl. Med.* **6**, 221ra15 (2014).
6. G. Sirokmány, Á. Donkó, M. Geiszt, Nox/duox family of NADPH oxidases: Lessons from knockout mouse models. *Trends Pharmacol. Sci.* **37**, 318–327 (2016).
7. R. P. Brandes, N. Weissmann, K. Schröder, Nox family NADPH oxidases: Molecular mechanisms of activation. *Free Radic. Biol. Med.* **76**, 208–226 (2014).
8. G. Groeger, A. M. Mackey, C. A. Pettigrew, L. Bhatt, T. G. Cotter, Stress-induced activation of Nox contributes to cell survival signalling via production of hydrogen peroxide. *J. Neurochem.* **109**, 1544–1554 (2009).
9. F. Jiang, G.-S. Liu, G. J. Dusting, E. C. Chan, NADPH oxidase-dependent redox signaling in TGF-β-mediated fibrotic responses. *Redox Biol.* **2**, 267–272 (2014).
10. S. Menegon, A. Columbano, S. Giordano, The dual roles of NRF2 in cancer. *Trends Mol. Med.* **22**, 578–593 (2016).
11. K. Schröder *et al*., Nox4 is a protective reactive oxygen species generating vascular NADPH oxidase. *Circ. Res.* **110**, 1217–1225 (2012).
12. M. Zhang *et al*., NADPH oxidase-4 mediates protection against chronic load-induced stress in mouse hearts by enhancing angiogenesis. *Proc. Natl. Acad. Sci. U.S.A.* **107**, 18121–18126 (2010).
13. S. M. Craige *et al*., Endothelial NADPH oxidase 4 protects ApoE-/- mice from atherosclerotic lesions. *Free Radic. Biol. Med.* **89**, 1–7 (2015).
14. E. Di Marco *et al*., NOX4-derived reactive oxygen species limit fibrosis and inhibit proliferation of vascular smooth muscle cells in diabetic atherosclerosis. *Free Radic. Biol. Med.* **97**, 556–567 (2016).
15. S. P. Gray *et al*., Reactive oxygen species can provide atheroprotection via NOX4-dependent inhibition of inflammation and vascular remodeling. *Arterioscler. Thromb. Vasc. Biol.* **36**, 295–307 (2016).
16. R. E. Clempus *et al*., Nox4 is required for maintenance of the differentiated vascular smooth muscle cell phenotype. *Arterioscler. Thromb. Vasc. Biol.* **27**, 42–48 (2007).
17. K. Schröder, K. Wandzioch, I. Helmcke, R. P. Brandes, Nox4 acts as a switch between differentiation and proliferation in preadipocytes. *Arterioscler. Thromb. Vasc. Biol.* **29**, 239–245 (2009).
18. C. Goettsch *et al*., NADPH oxidase 4 limits bone mass by promoting osteoclastogenesis. *J. Clin. Invest.* **123**, 4731–4738 (2013).
19. N. Jafari *et al*., CRISPR-Cas9 mediated NOX4 knockout inhibits cell proliferation and invasion in HeLa cells. *PLoS One* **12**, e0170327 (2017).
20. N. Sampson *et al*., Inhibition of Nox4-dependent ROS signaling attenuates prostate fibroblast activation and abrogates stromal-mediated protumorigenic interactions. *Int. J. Cancer* **143**, 383–395 (2018).
21. S. Tang, L. Yang, X. Tang, M. Liu, The role of oxidized ATM in the regulation of oxidative stress-induced energy metabolism reprogramming of CAFs. *Cancer Lett.* **353**, 133–144 (2014).
22. D. Chowdhury *et al*., gamma-H2AX dephosphorylation by protein phosphatase 2A facilitates DNA double-strand break repair. *Mol. Cell* **20**, 801–809 (2005).
23. M.-C. Keogh *et al*., A phosphatase complex that dephosphorylates gammaH2AX regulates DNA damage checkpoint recovery. *Nature* **439**, 497–501 (2006).
24. P. Cohen, S. Klumpp, D. L. Schelling, An improved procedure for identifying and quantitating protein phosphatases in mammalian tissues. *FEBS Lett.* **250**, 596–600 (1989).
25. R. Amaravadi, C. B. Thompson, The survival kinases Akt and Pim as potential pharmacological targets. *J. Clin. Invest.* **115**, 2618–2624 (2005).
26. A. Bellacosa, C. C. Kumar, A. Di Cristofano, J. R. Testa, Activation of AKT kinases in cancer: Implications for therapeutic targeting. *Adv. Cancer Res.* **94**, 29–86 (2005).
27. T. A. Millward, S. Zolnierowicz, B. A. Hemmings, Regulation of protein kinase cascades by protein phosphatase 2A. *Trends Biochem. Sci.* **24**, 186–191 (1999).
28. Y.-C. Kuo *et al*., Regulation of phosphorylation of Thr-308 of Akt, cell proliferation, and survival by the B55alpha regulatory subunit targeting of the protein phosphatase 2A holoenzyme to Akt. *J. Biol. Chem.* **283**, 1882–1892 (2008).
29. H. Murata *et al*., Glutaredoxin exerts an antiapoptotic effect by regulating the redox state of Akt. *J. Biol. Chem.* **278**, 50226–50233 (2003).
30. G. Krauss, Ed., *Biochemistry of Signal Transduction and Regulation* (Wiley-VCH, Weinheim, 2014).
31. M. Kiely, P. A. Kiely, PP2A: The wolf in sheep's clothing? *Cancers (Basel)* **7**, 648–669 (2015).
32. B. Perillo *et al*., ROS in cancer therapy: The bright side of the moon. *Exp. Mol. Med.* **52**, 192–203 (2020).
33. R. P. Brandes, N. Weissmann, K. Schröder, Redox-mediated signal transduction by cardiovascular Nox NADPH oxidases. *J. Mol. Cell. Cardiol.* **73**, 70–79 (2014).
34. A. C. Brewer *et al*., Nox4 regulates Nrf2 and glutathione redox in cardiomyocytes in vivo. *Free Radic. Biol. Med.* **51**, 205–215 (2011).
35. J. R. Burgoyne *et al*., Deficient angiogenesis in redox-dead Cys17Ser PKARIα knock-in mice. *Nat. Commun.* **6**, 7920 (2015).
36. J. R. Burgoyne, H. Mongue-Din, P. Eaton, A. M. Shah, Redox signaling in cardiac physiology and pathology. *Circ. Res.* **111**, 1091–1106 (2012).
37. T. F. Franke, D. R. Kaplan, L. C. Cantley, PI3K: Downstream AKTion blocks apoptosis. *Cell* **88**, 435–437 (1997).
38. M. Tanaka *et al*., Inhibition of NADPH oxidase 4 induces apoptosis in malignant mesothelioma: Role of reactive oxygen species. *Oncol. Rep.* **34**, 1726–1732 (2015).
39. Q. D. Zhao *et al*., NADPH oxidase 4 induces cardiac fibrosis and hypertrophy through activating Akt/mTOR and NFκB signaling pathways. *Circulation* **131**, 643–655 (2015).
40. C. Zhang *et al*., NOX4 promotes non-small cell lung cancer cell proliferation and metastasis through positive feedback regulation of PI3K/Akt signaling. *Oncotarget* **5**, 4392–4405 (2014).
41. E. Crosas-Molist *et al*., The NADPH oxidase NOX4 represses epithelial to amoeboid transition and efficient tumour dissemination. *Oncogene* **36**, 3002–3014 (2017).
42. Z.-M. Liu, H.-Y. Tseng, H.-W. Tsai, F.-C. Su, H.-S. Huang, Transforming growth factor β-interacting factor-induced malignant progression of hepatocellular carcinoma cells depends on superoxide production from Nox4. *Free Radic. Biol. Med.* **84**, 54–64 (2015).
43. J.-A. Choi, Y. S. Jung, J. Y. Kim, H. M. Kim, I. K. Lim, Inhibition of breast cancer invasion by TIS21/BTG2/Pc3-Akt1-Sp1-Nox4 pathway targeting actin nucleators, mDia genes. *Oncogene* **35**, 83–93 (2016).
44. M. Edderkaoui *et al*., NADPH oxidase activation in pancreatic cancer cells is mediated through Akt-dependent up-regulation of p22phox. *J. Biol. Chem.* **288**, 36259 (2013).
45. B. Govindarajan *et al*., Overexpression of Akt converts radial growth melanoma to vertical growth melanoma. *J. Clin. Invest.* **117**, 719–729 (2007).
46. H.-S. Zhang, W.-W. Sang, Z. Ruan, Y.-O. Wang, Akt/Nox2/NF-κB signaling pathway is involved in Tat-induced HIV-1 long terminal repeat (LTR) transactivation. *Arch. Biochem. Biophys.* **505**, 266–272 (2011).
47. A. K. Jayavelu *et al*., NOX4-driven ROS formation mediates PTP inactivation and cell transformation in FLT3ITD-positive AML cells. *Leukemia* **30**, 473–483 (2016).
48. R. Kodama *et al*., ROS-generating oxidases Nox1 and Nox4 contribute to oncogenic Ras-induced premature senescence. *Genes Cells* **18**, 32–41 (2013).
49. W. M. Bonner *et al*., GammaH2AX and cancer. *Nat. Rev. Cancer* **8**, 957–967 (2008).
50. W. Cui *et al*., NOX1/nicotinamide adenine dinucleotide phosphate, reduced form (NADPH) oxidase promotes proliferation of stellate cells and aggravates liver fibrosis induced by bile duct ligation. *Hepatology* **54**, 949–958 (2011).
51. K. Ito *et al*., Inhibition of Nox1 induces apoptosis by attenuating the AKT signaling pathway in oral squamous cell carcinoma cell lines. *Oncol. Rep.* **36**, 2991–2998 (2016).
52. A. S. Mondol, N. K. Tonks, T. Kamata, Nox4 redox regulation of PTP1B contributes to the proliferation and migration of glioblastoma cells by modulating tyrosine phosphorylation of coronin-1C. *Free Radic. Biol. Med.* **67**, 285–291 (2014).
53. S. Nlandu-Khodo *et al*., NADPH oxidase 4 deficiency increases tubular cell death during acute ischemic reperfusion injury. *Sci. Rep.* **6**, 38598 (2016).
54. I. Smyrnias *et al*., Nicotinamide adenine dinucleotide phosphate oxidase-4-dependent upregulation of nuclear factor erythroid-derived 2-like 2 protects the heart during chronic pressure overload. *Hypertension* **65**, 547–53 (2014).
55. F. Guo *et al*., Structural basis of PP2A activation by PTPA, an ATP-dependent activation chaperone. *Cell Res.* **24**, 190–203 (2014).
56. H. Fujiki, M. Suganuma, Tumor promotion by inhibitors of protein phosphatases 1 and 2A: The okadaic acid class of compounds. *Adv. Cancer Res.* **61**, 143–194 (1993).
57. R. Zimmerman *et al*., PP2A inactivation is a crucial step in triggering apoptin-induced tumor-selective cell killing. *Cell Death Dis.* **3**, e291 (2012).
58. W. Li *et al*., PP2A inhibitors induce apoptosis in pancreatic cancer cell line PANC-1 through persistent phosphorylation of IKKα and sustained activation of the NF-κB pathway. *Cancer Lett.* **304**, 117–127 (2011).
59. X. Li, A. Nan, Y. Xiao, Y. Chen, Y. Lai, PP2A-B56ε complex is involved in dephosphorylation of γ-H2AX in the repair process of CPT-induced DNA double-strand breaks. *Toxicology* **331**, 57–65 (2015).
60. S. Saikolappan, B. Kumar, G. Shishodia, S. Koul, H. K. Koul, Reactive oxygen species and cancer: A complex interaction. *Cancer Lett.* **452**, 132–143 (2019).
61. K. Roy *et al*., NADPH oxidases and cancer. *Clin. Sci. (Lond.)* **128**, 863–875 (2015).
62. G. S. López-Álvarez *et al*., Gene silencing of Nox4 by CpG island methylation during hepatocarcinogenesis in rats. *Biol. Open* **6**, 59–70 (2017).
63. S. Y. Ha *et al*., NADPH oxidase 1 and NADPH oxidase 4 have opposite prognostic effects for patients with hepatocellular carcinoma after hepatectomy. *Gut Liver* **10**, 826–835 (2016).

64. C.-L. Lu *et al*., NADPH oxidase DUOX1 and DUOX2 but not NOX4 are independent predictors in hepatocellular carcinoma after hepatectomy. *Tumour Biol.* **32**, 1173–1182 (2011).
65. E. Crosas-Molist *et al*., The NADPH oxidase NOX4 inhibits hepatocyte proliferation and liver cancer progression. *Free Radic. Biol. Med.* **69**, 338–347 (2014).
66. A. Sobhakumari *et al*., NOX4 mediates cytoprotective autophagy induced by the EGFR inhibitor erlotinib in head and neck cancer cells. *Toxicol. Appl. Pharmacol.* **272**, 736–745 (2013).
67. J. Stanicka, E. G. Russell, J. F. Woolley, T. G. Cotter, NADPH oxidase-generated hydrogen peroxide induces DNA damage in mutant FLT3-expressing leukemia cells. *J. Biol. Chem.* **290**, 9348–9361 (2015).
68. U. Weyemi *et al*., ROS-generating NADPH oxidase NOX4 is a critical mediator in oncogenic H-Ras-induced DNA damage and subsequent senescence. *Oncogene* **31**, 1117–1129 (2012).
69. M. A. Kang, E.-Y. So, A. L. Simons, D. R. Spitz, T. Ouchi, DNA damage induces reactive oxygen species generation through the H2AX-Nox1/Rac1 pathway. *Cell Death Dis.* **3**, e249 (2012).
70. G. Gavazzi *et al*., NOX1 deficiency protects from aortic dissection in response to angiotensin II. *Hypertension* **50**, 189–196 (2007).
71. F. el Marjou *et al*., Tissue-specific and inducible Cre-mediated recombination in the gut epithelium. *Genesis* **39**, 186–193 (2004).
72. F. Moll *et al*., NoxO1 controls proliferation of colon epithelial cells. *Front. Immunol.* **9**, 973 (2018).
73. F. Rezende *et al*., Cytochrome P450 enzymes but not NADPH oxidases are the source of the NADPH-dependent lucigenin chemiluminescence in membrane assays. *Free Radic. Biol. Med.* **102**, 57–66 (2017).
74. M. M. Bradford, A rapid and sensitive method for the quantitation of microgram quantities of protein utilizing the principle of protein-dye binding. *Anal. Biochem.* **72**, 248–254 (1976).
75. C. Riccardi, I. Nicoletti, Analysis of apoptosis by propidium iodide staining and flow cytometry. *Nat. Protoc.* **1**, 1458–1461 (2006).
76. D. Rübsamen *et al*., Inflammatory conditions induce IRES-dependent translation of cyp24a1. *PLoS One* **9**, e85314 (2014).
77. J. Clark *et al*., Quantification of PtdInsP3 molecular species in cells and tissues by mass spectrometry. *Nat. Methods* **8**, 267–272 (2011).
78. J. Rappsilber, M. Mann, Y. Ishihama, Protocol for micro-purification, enrichment, prefractionation and storage of peptides for proteomics using StageTips. *Nat. Protoc.* **2**, 1896–1906 (2007).
79. M. Götze *et al*., StavroX–A software for analyzing crosslinked products in protein interaction studies. *J. Am. Soc. Mass Spectrom.* **23**, 76–87 (2012).
80. M. A. Ashwell *et al*., Discovery and optimization of a series of 3-(3-phenyl-3H-imidazo [4,5-b]pyridin-2-yl)pyridin-2-amines: Orally bioavailable, selective, and potent ATP-independent Akt inhibitors. *J. Med. Chem.* **55**, 5291–5310 (2012).
81. J. Cox, M. Mann, MaxQuant enables high peptide identification rates, individualized p.p.b.-range mass accuracies and proteome-wide protein quantification. *Nat. Biotechnol.* **26**, 1367–1372 (2008).
82. S. Tyanova *et al*., The Perseus computational platform for comprehensive analysis of (prote)omics data. *Nat. Methods* **13**, 731–740 (2016).